npj | climate and atmospheric science

Article

Published in partnership with CECCR at King Abdulaziz University

https://doi.org/10.1038/s41612-025-01067-z

Hourly extreme rainfall projections over South Korea using convection permitting climate simulations

Ga-Yeong Seo[1], Seung-Ki Min[1,2] ✉, Donghyun Lee[3], Seok-Woo Son[4], Chanil Park[5] & Dong-Hyun Cha[6]

This study analyzes the impact of climate change on the summertime hourly extreme rainfall event (HER) over South Korea. The UKESM-forced regional climate model is utilized to simulate HER over South Korea in the historical (2001–2005) and future periods (2091–2095) under the SSP1-2.6 and SSP5-8.5 scenarios at a convection-permitting resolution (2.5 km). A significant increase in future HER intensity and frequency appears in July, with the frequency increases about two times for SSP1-2.6 and about 3.7 times for SSP5-8.5 scenarios. The month of maximum HER frequency is also projected to shift from August to July. When clustering the HERs into six representative weather patterns, SSP5-8.5 scenarios show a predominant increase in weather patterns characterized by a frontal boundary between low and high pressure in July. Our results suggest that the future sub-seasonal evolution of HER over South Korea may change with the intensification of subtropical high and the deepening of mid-level trough according to different future scenarios.

Extreme rainfall event is one of the most crucial meteorological phenomena which have great influences on ecosystems and human society. It causes natural disasters, such as floods or landslides, and leads to loss of life and property damage. In the past 4 years, extreme rainfall events have occurred every year in South Korea, resulting in over 150 casualties and extensive property damages[1,2]. It can be inarguably asserted that the frequent occurrence of extreme rainfall events in recent years is linked to climate change. The impact of climate change on extreme rainfall has been reported by previous studies based on observed long-term trend analyses[3–6] and future climate simulations[7–13]. These studies argued that a significant increase of short-duration extreme rainfall events is evident, and the percentage changes in both frequency and intensity will be even greater in the future, especially for more severe rainfall. Despite an increasing attention paid to sub-daily extreme rainfall, however, detailed future projections of extreme rainfall are not well quantified.

The utilization of regional climate model (RCM) is necessary in simulating a local extreme climate. However, conventional RCMs, with a horizontal resolution of tens of kilometers, often have difficulties in simulating localized extreme rainfall events due to rather coarse resolution. To overcome this limitation, a high-resolution (≤4 km) RCM has recently been proposed[14,15]. This modeling approach allows the deactivation of error-prone cumulus parameterization schemes, referred to as convection-permitting model (CPM). The advantages of CPM in simulating sub-daily rainfall have been highlighted with improved representation of rainfall intensity and diurnal cycle, as it can explicitly simulate the deep convection process[14,16–19]. This leads to an improvement in short-duration extreme rainfall modeling performance[12,20–22]. The CPM also exhibits a better performance in simulating precipitation over regions of complex terrain[21,23,24] and high-elevation[25,26] owing to the realistic representation of topography. However, most previous studies have focused on the characteristics of rainfall over long-term or seasonal periods.

Various features of extreme rainfall events appear in South Korea owing to complex atmospheric factors[6,27–29]. Changma, a subsystem of the East Asian summer monsoon, has a great influence on precipitation patterns over South Korea in early summer[30,31]. Changma often brought a prolonged rainy period to South Korea with a quasi-stationary front, but it has been undergoing changes owing to climate change in recent years, prompting research for its redefinition[32]. In late summer, extreme rainfall events in South Korea are also associated with tropical cyclones and mid-latitude flow. Moreover, the complex topography of South Korea contributes to the spatial variability of rainfall. Therefore, it is necessary to

---

[1]Division of Environmental Science and Engineering, Pohang University of Science and Technology, Pohang, South Korea. [2]Institute for Convergence Research and Education in Advanced Technology, Yonsei University, Seoul, South Korea. [3]Department of Physics, Imperial College London, London, UK. [4]School of Earth and Environmental Sciences, Seoul National University, Seoul, Republic of Korea. [5]Department of Earth and Environmental Sciences, Boston College, Chestnut Hill, MA, USA. [6]Department of Civil, Urban, Earth, and Environmental Engineering, Ulsan National Institute of Science and Technology, Ulsan, South Korea.
✉e-mail: skmin@postech.ac.kr

understand the characteristics of rainfall patterns in South Korea on various spatial and temporal scales.

In this study, we aim to examine future changes of the hourly scale extreme rainfall events in South Korea under two different future emission scenarios by utilizing the CPM. In particular, we explore the monthly variations of summertime hourly extreme rainfall, focusing on its frequency. First, the added-value of the high-resolution CPM is assessed for historical climate simulations in view of observations. Then, we examine the changes in extreme rainfall patterns under climate change by analyzing the frequency of extreme rainfall events according to the weather patterns.

Results

Future changes in monthly variation of hourly extreme rainfall event (HER)

Before projecting future climate, the performance of the 2.5 km resolution CPM (CPM2.5) in simulating extreme rainfall is briefly evaluated in comparison to the 25-km resolution RCM (RCM25). Figure 1a–c presents the features of hourly precipitation rainfall derived from observations and model results with CPM2.5 and RCM25 in historical and future periods. The CPM2.5 shows a better performance compared to the RCM25 for extreme precipitation above the 98th percentile (Fig. 1a–c). CPM2.5 results align more closely with observations with a bias of 13%, remarkably lower than RCM25 which shows 41% bias. The magnitude of the model biases between 99.90 and 99.99th percentile ranges from 9.9 to 19.5 mm and 3.3 to 6.0 mm for RCM25 and CPM2.5, respectively, indicating the added-value of CPM for reproducing the observed extreme rainfall distributions. Future climate projections exhibit high precipitation amount over 99.90th percentile compared to the historical with increases of about 14% and 60% under the SSP1-2.6 (SSP126) and SSP5-8.5 scenarios (SSP585), respectively. In SSP585 scenario, the increase becomes steeper above 99.93rd percentile.

Figure 1d, e shows the frequency and mean precipitation amount of hourly rainfall event exceeding the 99.95th percentile for each month. The observations show the relatively high frequency in July and August, but there is little difference in rainfall amounts between the months (34.3–37.9 mm/h). The model results obtained through bootstrapping are analyzed based on the median. Both CPM2.5 and RCM25 overestimate frequency in June and underestimate the precipitation amount of extreme rainfall events, but can capture the observed monthly variations of historical extreme rainfall events. Compared to RCM25, CPM2.5 simulates the monthly variation of extreme rainfall frequency close to the observations, especially by reducing about 70% of RCM25 biases in August. For the precipitation intensity, rainfall amount simulations are clearly improved in CPM2.5 compared to RCM25. These results support the added-value of high-resolution modeling simulation[17,24]. Future scenarios show increases in both the frequency and intensity for all summer month under SSP585, whereas SSP126 exhibits varying patterns across different months. In July and August, which account for most of the summer precipitation, the changes are more evident in frequency than in precipitation amount.

Using the CPM2.5 simulations, we project the future changes of the monthly and sub-daily HER frequency (Fig. 2). Here, HER is defined as the cases where the hourly-accumulated rainfall amount exceeds the 99.95th percentile historical period rainfall over the land region of South Korea (See Data and Methods). The average annual frequencies of HER are 56, 67, and 126 for historical, SSP126 and SSP585 scenarios, respectively. This indicates

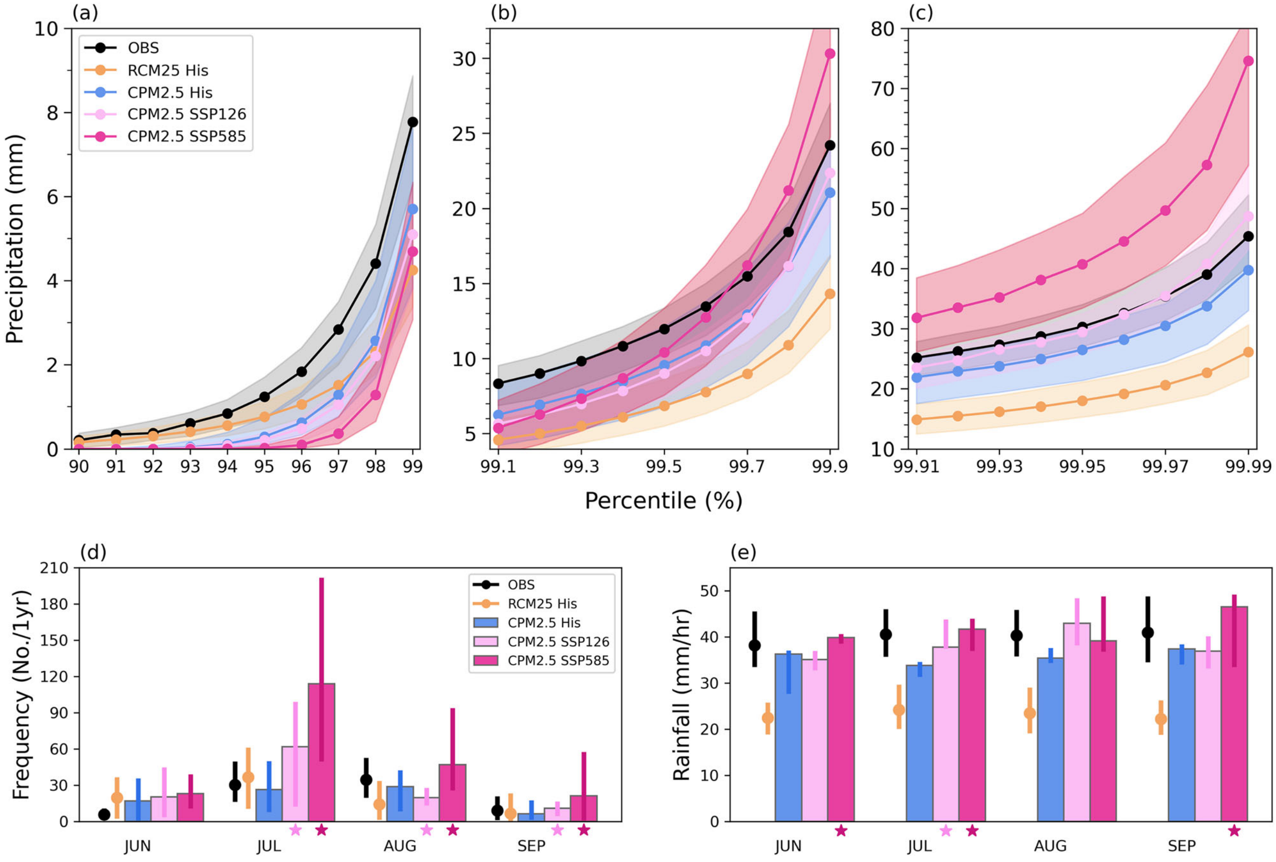

Fig. 1 | Assessment of regional climate model performance in simulating extreme rainfall over South Korea. a–c Hourly precipitation amount according to the percentile in historical and future period. Note that y-axis scales are different. **d** Frequency and **e** mean amount of rainfall events exceeding the 99.95th percentile derived from observation and model data in historical and future period. CCLM rainfall results are from data interpolated into ASOS stations. Results from the observation and RCM25 are presented for the historical period, while CPM2.5 are shown for both the historical and future periods. The shaded range in (**a**–**c**) and vertical lines in (**d**, **e**) indicate the 90% confidence interval diagnosed by the bootstrapping method. Star markers in (**d**, **e**) indicate the future changes are statistically significant at 99% confidence level in Wilcoxon rank-sum test.

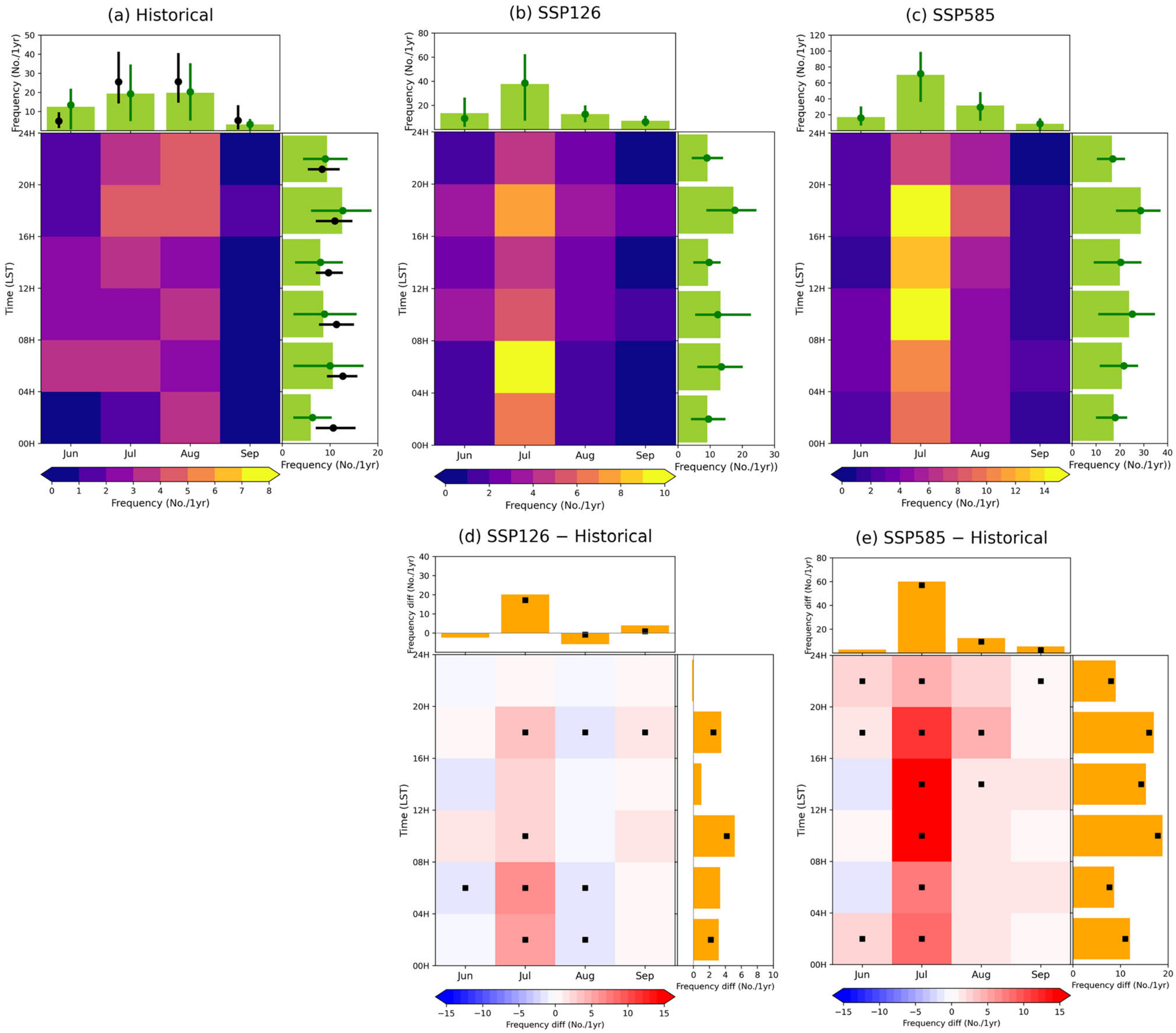

Fig. 2 | Monthly and diurnal variation of HER frequency. **a–c** Frequency of extreme rainfall event according to the month and local standard time (LST) (shaded) and monthly and diurnal variation of extreme rainfall event frequency (bar plot) under **a** Historical, **b** SSP126, and **c** SSP585 and their future changes under **d** SSP126 and **e** SSP585. Note that y-axis scales for bar plots are different. The black line and green line in (**a–c**) indicate the 90% confidence interval for the observation and CPM2.5 data, respectively, diagnosed by the bootstrapping method. Black square markers in (**d, e**) indicate the future changes are statistically significant at 99% confidence level in Wilcoxon rank-sum test.

that the HER frequency is projected to increase by approximately 18% under SSP126 and 123% under SSP585. In the historical period, the simulated HER frequency is within the observed range, although it is underestimated except in June (top subpanel in Fig. 2a). The highest frequency occurs in August with a diurnal peak at 16–24 LST and the second-highest monthly rainfall frequency appears in July, with only a slight difference between the two months. The bimodal diurnal peaks of summer HER occurrence which appear in the early morning and evening hours are consistent with observations[33,34]. The monthly peak in August (Fig. 2a) is projected to shift to July in future (Fig. 2b, c). Significant changes in HER frequency are found in July with a 99% increase under SSP126 and a 271% increase under SSP585.

Future changes in HER frequency are presented in Fig. 2d, e. Under SSP126, the HER frequency decreases in June (−32%) and August (−38%), whereas it increases in July and September to the much greater extent in July (Fig. 2d). The future changes in diurnal variation of HER frequency vary across different hour, and distinctive increase appears at 08–12 LST. The HER frequency change under SSP585 is positive for all months and hours and shows a much larger increase compared to the SSP126 (Fig. 2e). More than half of HERs are projected to occur in July with 271% increase while 46% increase is projected in August. In July, diurnal variation in HER frequency shows a double peak in the early morning (08–12 LST) and afternoon (16–20 LST) and the HER frequency peak also appears in the late afternoon in August (Fig. 2c). Under SSP585, the frequency increases significantly across the overall time of the day in July (Fig. 2e).

In the case of HER precipitation, it is projected to increase in both July (17.0–19.8%) and August (9.2–11.9%) in August under the SSP126 scenario, although the frequency of HER events decreased in August. A similar increasing pattern is projected under the SSP585 scenario, with increases of 16.7–24.0% in July and 9.0–22.2% in August. Therefore, to analyze the regional changes in future rainfall, the spatial distributions of precipitation anomalies when HER occurs are displayed in Fig. 3. The anomalies are calculated by subtracting climatological precipitation mean from the HER precipitation amount for the relevant period. The maximum HER precipitation is located in the southern (June and September) and northern (July and August) regions of South Korea in the historical period (Fig. 3a–e). The overestimation of HER event frequency in June is likely due to the

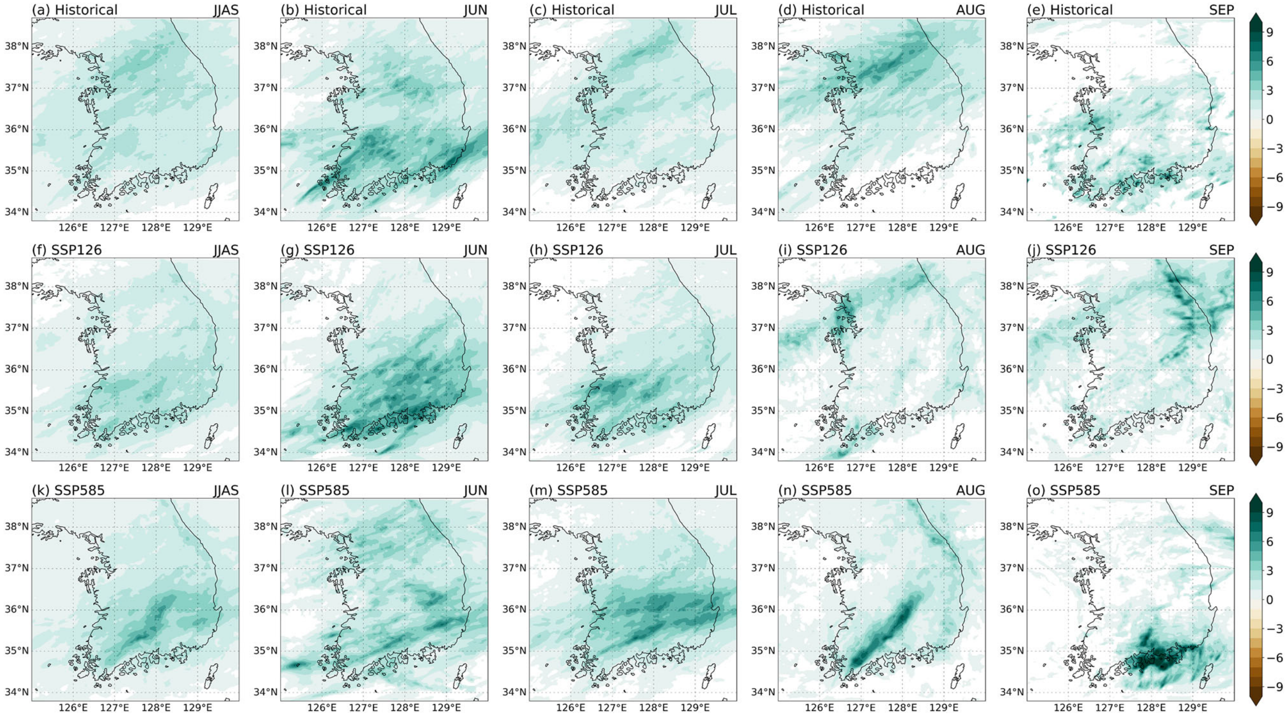

Fig. 3 | Spatial distribution of HER precipitation anomaly. Composite of HER precipitation anomaly (Units: mm/h) in (**a**, **f**, **k**) summertime (June–September), **b**, **g**, **l** June, **c**, **h**, **m** July, **d**, **i**, **n** August, and **e**, **j**, **o** September under **a**–**e** Historical, **f**–**j** SSP126, and **k**–**o** SSP585. The anomalies for summertime are calculated by subtracting summertime climatological precipitation mean from the HER precipitation amount in summertime. The anomalies for each month are calculated by subtracting monthly climatological precipitation mean from the HER precipitation amount for that month. Only unique HER hours are considered.

overestimation of precipitation over the southeastern region when compared with the observations (not shown). Both SSP126 and SSP585 results exhibit an increase of summer precipitation over the southern region of South Korea (Fig. 3a, f, k). In August under SSP585, a narrow diagonal precipitation band pattern appears, which is likely due to the mountainous topography of the region. The characteristics of CPM models to simulate intense precipitation over mountainous areas has also been reported in previous studies[24,35].

The relatively smaller rate of increase in precipitation in July compared to the rate of increase in frequency aligns with the results shown in Fig. 1d, e. In July, a greater increase in precipitation with wider area of the southern region appears under a higher emissions scenario (Fig. 3h, m). The spatial distribution of HER frequency presents that a relatively high frequency also appears over the southern region (Supplementary Fig. 1). Compared to August, both the rate of increase in rainfall amount and the frequency of HER events are higher in July resulting in a shift in the peak. Since HERs are events based on spatiotemporal pooling, we analyze the future changes in HER events over temporal and spatial scales (Supplementary Fig. 2). The frequency of HERs at individual ASOS stations exhibits a clear increase under higher concentration scenarios (SSP126: 30.3%, SSP585: 115.4%). In contrast, the number of ASOS stations with increased HER events per day shows relatively smaller differences between the historical and future period. These results indicate that the notable increase in HER frequency is primarily due to more frequent occurrences in the southern region. The HER precipitation in August diminishes under SSP126 over south of 37°N area, but it increases regionally under SSP585 (Fig. 3i, n). In September, the precipitation core is located in a different region according to the scenarios, suggesting the dominant occurrence of local HERs (Fig. 3j, o).

Future changes in HER according to the weather patterns

The above results indicate a shift of the HER peak from August to July with a significant increase in HER frequency in future climate. We next examine which weather pattern mostly contributes to this shift. Six weather patterns are identified by Self Organizing Map (SOM) method (see Data and Methods). They are derived from the observed 1894 HERs for 30 years over 1985–2014. The identified weather patterns agree with the previous results[36]. Figure 4a–f shows the composite of 850-hPa geopotential height when HERs occur for each cluster and we analyzed the weather patterns based on their similarity. For clusters 1 and 3 (hereafter C1 and C3), relatively low geopotential height anomaly in high latitudes and high anomaly in low latitudes are found (see also Supplementary Fig. 3). In contrast, C2 and C5 are dominated by relatively low pressure over the south and southwest of South Korea. According to the Park et al.[36], C1 and C3 represent a quasi-stationary frontal boundary between low and high pressure. The robust southwesterly integrated water vapor transport enters South Korea, transporting warm and humid air which induces the development of HER. C2 and C5 clusters are identified as extratropical cyclone pattern. As the cyclone system moves in from eastern China, it influences extreme rainfall development while positioned near the west region of South Korea during HER occurrences. When considering the position of the 500 hPa trough, the cyclone is tilted westward, indicating baroclinic instability. C4 shows a pattern where the edge of the North Pacific high is positioned over South Korea. In contrast to the patterns of C1 and C3, C4 shows a more pronounced North Pacific high influence compared to the low-pressure influence in the north. The strong moisture flux is transported along the edge of the expanded North Pacific high. The extreme rainfall events related to the C4 are usually triggered by a local disturbance on the boundary between low and high[36]. C6 presents a dominant high geopotential height pattern. Park et al.[36] found that diverse systems, like local instability or meso-α to synoptic-scale cyclone, are occasionally involved in C6.

The HER frequency for each cluster is presented in Fig. 4g–i. In historical period, main occurrence period differs from one cluster to another (Fig. 4g). The HER frequency for C1 and C3 is maximum in early summer, whereas that for C2 and C5 is found in July and August. In the case of C6, a noticeable HER occurrence in September is found. These features are similar to the observation results (not shown). In future climate, the HER frequency

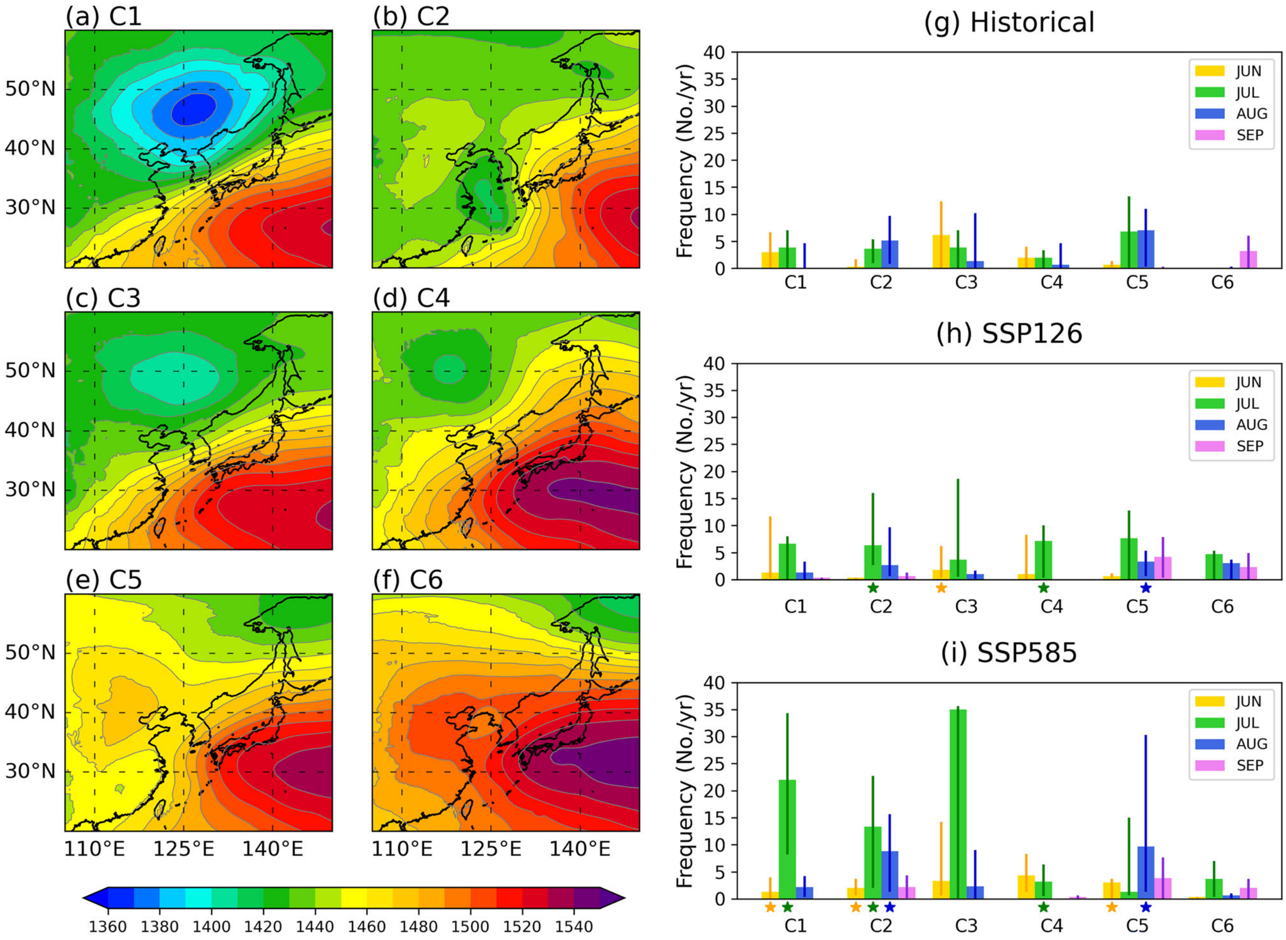

Fig. 4 | Characteristics of HER for each cluster. a–f Composite of observed geopotential height at 850 hPa (Units: **m**) for a Cluster 1 (C1), **b** Cluster 2 (C2), **c** Cluster 3 (C3), **d** Cluster 4 (C4), **e** Cluster 5 (C5), and **f** Cluster 6 (C6). Only unique HER hours are considered. **g–i** Frequency of HER for each month and cluster under **g** Historical, **h** SSP126, and **i** SSP585. The vertical line in (**g–i**) indicates the 90% confidence interval for the CPM2.5 data diagnosed by the bootstrapping method. Star markers in (**g-i**) indicate the future changes are statistically significant at 99% confidence level in Wilcoxon rank-sum test.

in July rapidly increases in specific weather patterns and shows different characteristics between SSP126 and SSP585 (Fig. 4h–i). Under SSP126, the highest HER frequency is found in July across all clusters. The July HER particularly shows a significant increase in C4 (259%) and C2 (72%). On the other hand, a HER decrease in August appears across all patterns except C1 and C6. Under SSP585, a high increase in July HER frequency is found in C1 and C3 with 474% and 814% increases, respectively. However, it should be noted that the frequency for C3 shows large uncertainty under both future scenarios. In August, the significant HER change is found in C2 and C5. The C1 + C3 pattern in July is projected to increase by approximately 644%, while the C2 + C5 pattern in August is expected to increase by about 52%.

Figure 5 shows the histogram of HER rainfall in July and August for each cluster. When examining future climate, HER frequency primarily increases for precipitation below 60 mm in July C2, C3, and C4 under SSP126. In C3, around ten occurrences of precipitation intensities not recorded in the historical climate occasionally appear. Similar to SSP126, most HERs in C2 and C5 under SSP585 are within the 30–40 mm range which is similar to the historical rainfall intensity. The HER frequency increases in C1 and C3 in response to an increased rainfall intensity. In August, most HERs are distributed in below 50 mm under SSP126, but interestingly, relatively high rainfall intensity HERs (above 70 mm) appears in C5 and C6. Although the increase in frequency of high-intensity HERs is not as high as that of the 30–50 mm range, it is noteworthy that the unprecedented high-intensity rainfall events are projected to emerge in future climate. Under SSP585, the HER frequency in C2 increases within the historical rainfall intensity range. While in C5, the frequency of high-intensity HERs notably increases, indicating the intensification of extreme rainfall. Consequently, in August under SSP585, the clusters of extratropical cyclone patterns which show high rate of increase exhibit different change features: C2 increases mainly in 30–40 mm rainfall, while intense precipitation HERs increase in C5.

The synoptic patterns associated with HER are further analyzed for each month to identify the factors responsible for the monthly changes in the frequency for each cluster. Figure 6 shows the geopotential height at 850 and 500 hPa and integrated water vapor transport (IVT) derived from RCM25. Here IVT is defined as follows.

$$IVT = \left(-\frac{1}{g}\int_{1000hPa}^{300hPa} uq\,dp\right)i + \left(-\frac{1}{g}\int_{1000hPa}^{300hPa} vq\,dp\right)j$$

where u and v are zonal and meridional wind (m/s), respectively, g is the gravitational acceleration, and q is a specific humidity (kg/kg). p is the pressure, i and j are zonal and meridional unit vector, respectively.

In July, distinct moisture transport patterns emerge in the historical period, with slight changes in future climate. In SSP126, the geopotential height increases over north region of western North Pacific, indicating the expansion of the high-pressure system to the north. This pattern is associated with an increase in the frequency of C4 under SSP126. SSP585 shows the development of a subtropical high over the western North Pacific in July. It creates a strong gradient of geopotential height on the east of South Korea, leading to a strong southerly IVT toward South Korea. The pattern is closely related to

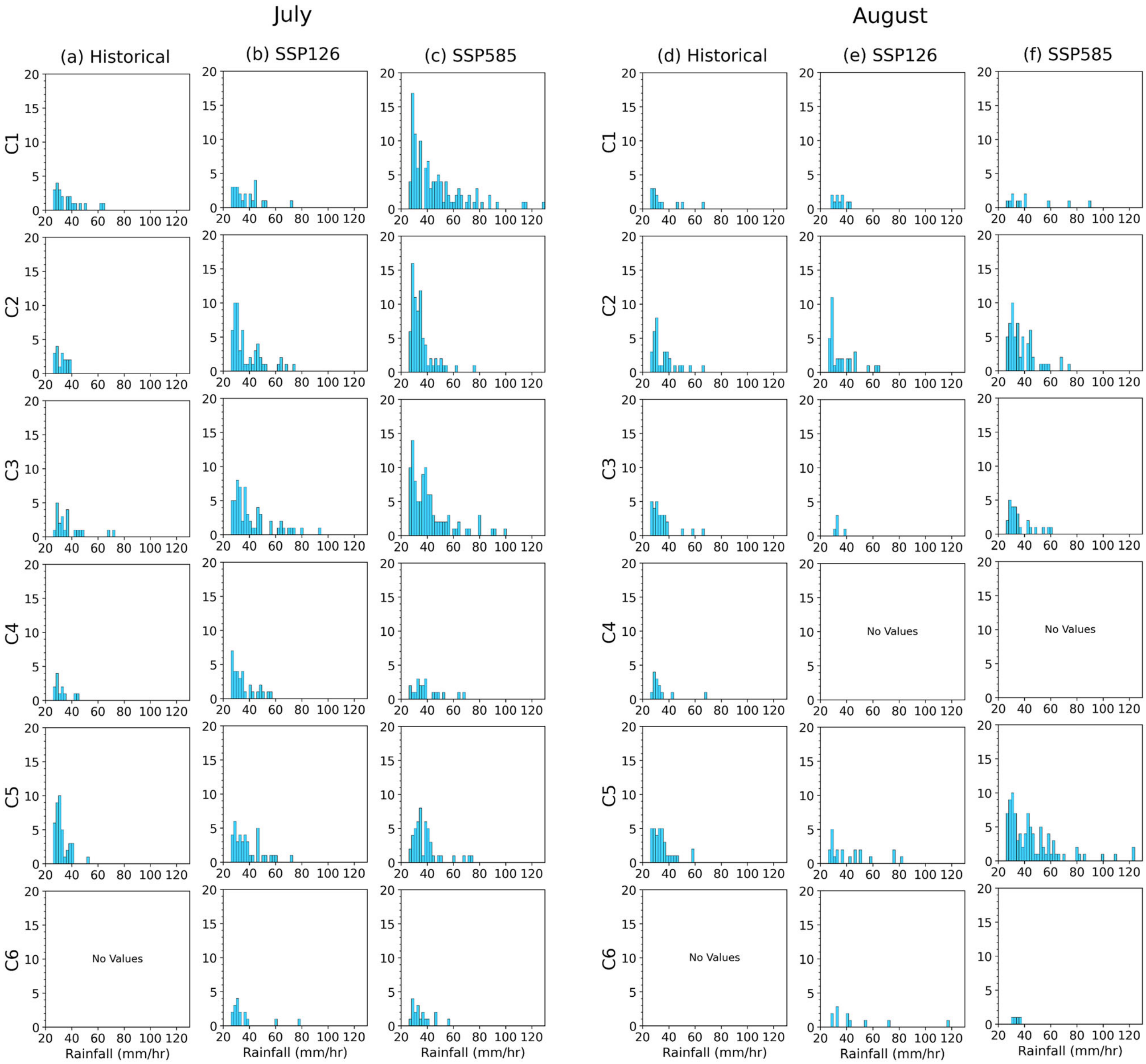

Fig. 5 | Histogram of HER rainfall amount. Histogram of HER rainfall amount (mm/h) for each cluster in (**a**–**c**) July and (**d**–**f**) August under **a**, **d** Historical, **b**, **e** SSP126, and **c**, **f** SSP585. The width of the bin is 2 mm. The results are the medians based on bootstrapping.

C1 and C3 where the front appears over South Korea. The patterns of C1 and C3 in July also represent the enhanced subtropical high with increased gradient over the western North Pacific (Supplementary Fig. 4). This result indicates that the development of the subtropical high over the western North Pacific contributes to the increasing July HER frequency in a warming climate. However, the development pattern varies between the future scenarios leading to differences in the clusters with increased frequency, where C4 frequency increases under SSP126 while C1 and C3 frequencies increase under SSP585 (Fig. 6b, c). In August, a difference is found between SSP126 and SSP585. While a 500-hPa trough develops over the northwest of South Korea under SSP585, a flat and similar circulation pattern to the historical period is found under SSP126 (Fig. 6e, f). The former pattern is also detected in July and it can influence the development of a low pressure near South Korea in lower troposphere, as in C2 and C5, under SSP585. This result suggests that the increasing C2 and C5 HER in July and August under SSP585 are mostly likely due to the development of a mid-level trough. Under SSP126, C2 + C5 pattern HER decrease in August, presumably due to the lack of a well-developed mid-level trough compared to the historical period (Supplementary Fig. 5).

The diurnal variation of HER frequency in July and August is further examined in Fig. 7. The diurnal variation of July HER in the historical period shows no significant difference among six clusters (Fig. 7a–f). The convective HER with high convective instability (see Data and Methods section) mostly occurs in the afternoon hours, with higher frequency in August compared to July. The afternoon convective HER which is accompanied with deep convection is usually modulated by the local surface heating[34], implying its sensitivity to the magnitude of future temperature changes. In future climate, each cluster exhibits prominent increase in its frequency. For July HER under SSP126, small increase appears in the afternoon for C4 which is the cluster with high increase rates. (Fig. 7j). As the total number of HER frequency increases, the proportion of convective HER also rises in the afternoon hours from 6.7 to 11.0% (Table 1). Under SSP585, C3 occurs more frequently in the between 04 and 16 LST compared to the historical period and a significant increase in C1 is evident in the afternoon. The convective HER in July notably increases in the afternoon hours for these clusters, accounting for 20.1% of the total HERs. In August, the frequency of

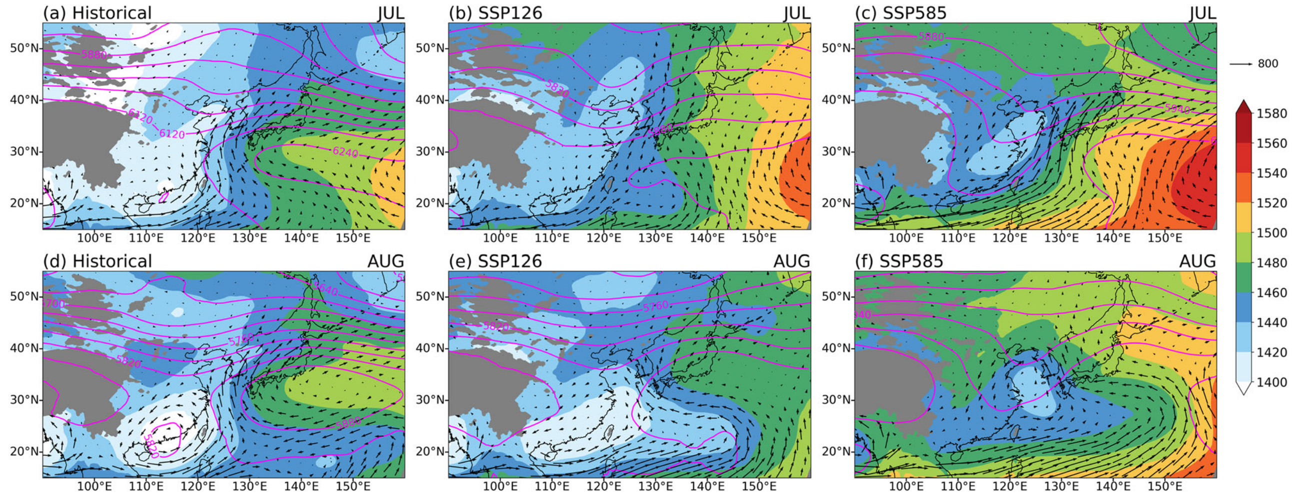

Fig. 6 | Weather patterns of HER for each month. Composite map of integrated water vapor transport (Units: kg·m^{-1}s^{-1}; vector) and geopotential height at 850 hPa (Units: m; shaded) and 500 hPa (Units: m; pink contour) for HERs in **a**–**c** July, and **d**–**f** August under **a**, **d** Historical, **b**, **e** SSP126, and **c**, **f** SSP585. Only unique HER hours are considered. The integrated water vapor transport and geopotential height at 850 hPa are masked where the altitude above 1500 m.

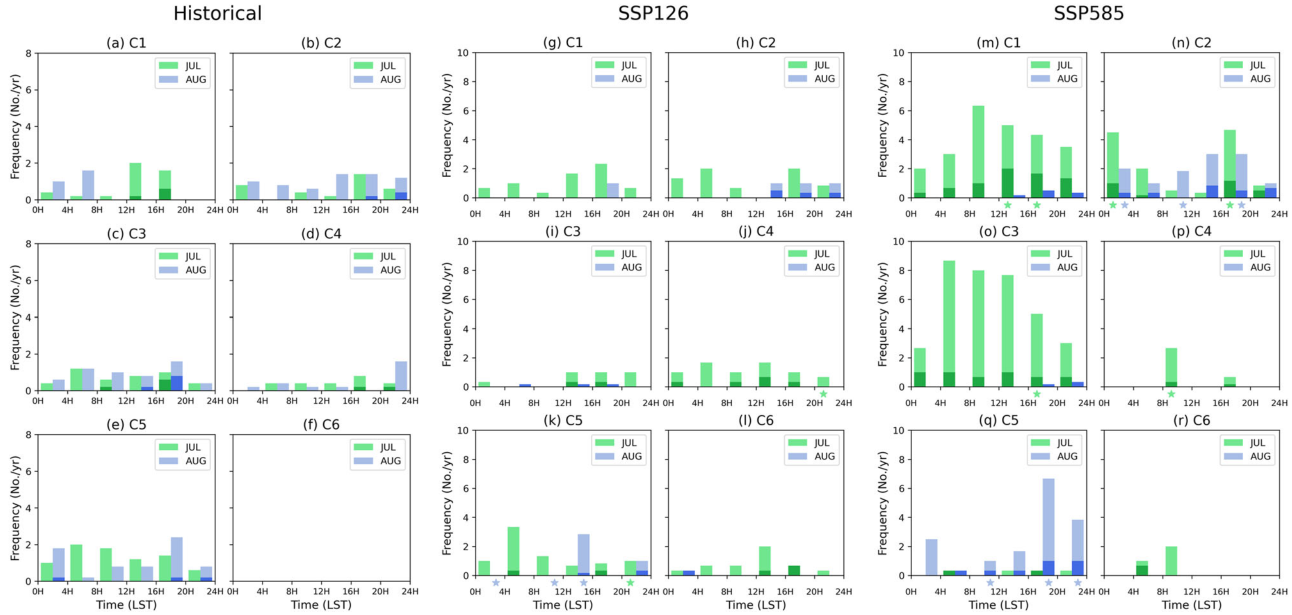

Fig. 7 | Diurnal variation of HER and convective HER frequency. Frequency of HER (light color) and convective HER (dark color) in July (green color) and August (blue color) according to the clusters under **a**–**f** Historical, **g**–**l** SSP126, and **m**–**r** SSP585. The frequencies are calculated at 4-h intervals and the results are the medians obtained based on bootstrapping. Star markers in (**g**–**r**) indicate the future changes of HER frequency are statistically significant at 99% confidence level in Wilcoxon rank-sum test.

SSP126 and SSP585 HER is higher in the afternoon hours for C2 and C5. Under SSP585 scenario, the convective rainfall events dramatically increase in the afternoon hours, with proportion of afternoon convective HER events rising from 10.4% to 29.8%. The annual mean convective HER frequency in summertime is projected to increase in future climates with higher greenhouse gas emission scenarios (SSP126: 27%, SSP585: 145%), resulting in a larger share of total HERs. Consequently, the role of CPM that can explicitly simulate deep convection is expected to become more important for the future projection of extreme rainfall.

Discussion

This study analyzes the future changes in hourly scale extreme rainfall (HER) events according to the weather patterns in South Korea under SSP126 and SSP585 scenarios utilizing a high-resolution convection permitting model. The regional climate model is used to conduct experiments for dynamically downscaling at 25 km and 2.5 km by one-way nesting. The 2.5 km convection permitting resolution results (CPM2.5) show better performances in simulating extreme rainfall compared to the 25 km mother domain results (RCM25). The CPM2.5 model simulates both the frequency and intensity of South Korean hourly extreme rainfall in summertime reasonably, aligning closely with the observations and reducing the bias of the RCM25 by about 70%.

The total HER frequency is expected to increase in the future climate under global warming, but the monthly changes differ according to future emission scenarios. The highest frequency of HER is recorded in August in the historical climate, but the monthly peak is projected to shift from August to July in the future climate. A significant HER frequency increase appears in July under both SSP126 and SSP585 with 99% and 271% increases,

Table 1 | The percentage of convective HER within the total HERs

Scenario	Month	Morning hours (00–12 LST)	Afternoon hours (12–24 LST)
Historical	July	1.0%	6.7%
	August	0.0%	10.4%
SSP126	July	6.3%	11.0%
	August	12.5%	19.4%
SSP585	July	14.8%	20.1%
	August	18.8%	29.8%

Note that the values are the medians obtained through bootstrapping

Table 2 | Configuration of CCLM regional climate model

	RCM25	CPM2.5
Model domain	East Asia	South Korea
Horizontal resolution	25 km	2.5 km
Cumulus scheme	Tiedtke	OFF
Microphysics scheme	Extended DM	
Radiation scheme	Ritter-Geleyn	
Land surface model	TERRA_ML	
Spectral nudging	ON	OFF

respectively. In August, HER frequency also increases under SSP585, whereas a decrease appears under SSP126. By clustering the weather patterns related to the HER, we find out which synoptic pattern contributes to the shift of the peak. The frequency of HER in July of C2 and C4 significantly increases under SSP126 (72% and 259%, respectively), due to the northward expansion of the western North Pacific subtropical high compared to the historical climate. Under SSP585, the frequency of the quasi-stationary frontal patterns (C1 + C3) increases by 644% in July, indicating that the large increase in July HER occurrence in C1 and C3 impacts to the monthly frequency peak in July. The positive changes of HER frequency in August under SSP585 are influenced by a significantly frequency increase for extratropical cyclone patterns (C2 + C5). The future changes in HER frequency by intensity are not evident with regard to the weather patterns, but the distinct characteristics in HER intensity according to the future scenarios can be identified. Because the convective HER is generally featured as short-duration, high-intensity rainfall, the importance of reliable future projection utilizing CPM is being emphasized. The diurnal variation of HER shows different increase patterns according to the future climates, with SSP126 displaying a prominent rise in the afternoon for C2 and C4 in July, and SSP585 exhibiting increases in both morning and afternoon hours. Under SSP585, convective rainfall events increase sharply in the afternoon in August (430%), especially in C2 + C5 patterns.

The factors affecting monthly changes according to weather patterns can be identified through the changes in monthly synoptic patterns in future climate. In July, the intensification of high pressure over the western North Pacific region contributes to the increased frequency of C4 under SSP126 and C1 and C3 under SSP585. In August, the deepening of mid-level trough appears only under SSP585, inducing the development of a low-level low-pressure near South Korea, which contributes to the increased frequency of C2 and C5. The increase of western North Pacific subtropical high intensity is the main point leading to the future changes of monthly variation in HER frequency. This increment also appears in UKESM data, indicating that the RCM results are directly influenced by the boundary forcing data. UKESM has been known to have reasonable performance in simulating extreme precipitation[37], but it tends to estimate large temperature increase which may contribute to the intensified western North Pacific subtropical high in future projection[38,39].

Previous studies have shown the large uncertainty in future changes of the western North Pacific subtropical high in CMIP5 and CMIP6 data[40–42]. However, projections based on emergent constraints suggest a robust intensification of the western North Pacific subtropical high in future[43], implying possible increases of the HER frequency associated with the quasi-stationary front pattern. In addition, the increase of geopotential height in western North Pacific is considered to be due to the development of an El Niño-like warming pattern in the future climate[44]. Reflecting the strong correlation between the western North Pacific subtropical high and tropical sea surface temperature, a comprehensive understanding of the mechanisms associated with these two climatic phenomena is required for more reliable projections of HER.

This study has significance in quantitatively analyzing the monthly-dependent response of hourly extreme rainfall frequency changes under various future climate change scenarios. Importantly, using improved high-resolution simulations of convective extremes, we show that higher emissions will bring substantial increases in the frequency and intensity of short-duration extreme rainfall events, demonstrating the potentially huge benefits in the East Asian monsoon region obtained by global warming mitigation. Although there remain uncertainties arising from the single-model based future projections, previous multi-model studies have also shown a notable increase in extreme precipitation in July compared to other summer months under future climate conditions[45,46]. In addition, this study focused on how different emission scenarios affect the HER and related weather patterns, highlighting the specific role of greenhouse gas concentrations under controlled conditions.

Our synoptic pattern analysis indicates that large-scale mechanisms associated with the enhanced subtropical high in the western North Pacific are consistently at work, inducing the distinct changes in hourly extreme rainfall events. In particular, the expansion of the western North Pacific subtropical high is expected to play a crucial role in the combined effect between HER-related weather patterns, influencing the path of IVT in C1 and C3 patterns and modifying the boundary location of subtropical high in C4 pattern, which in turn affects the characteristics of extreme rainfall events. Future works are required to explore and quantify the potential influences of other forcing factors like land-use changes or aerosol interactions. While this study focuses on climatological HER-related weather patterns, unprecedented new weather patterns may emerge in future climate. When we perform SOM clustering analysis on future climate data, some new weather patterns are identified. However, their underlying mechanisms of precipitation development are largely consistent with those observed in the historical climate. Therefore, we assign these HERs with similar historical patterns. Further investigation into the characteristics of these newly emerging patterns appears to be necessary. In addition, detailed dynamics of extreme rainfall events, and the interactions between the HER-related synoptic patterns need to be further explored given the multifaceted nature of climate systems.

Data and Methods

Model description

The Consortium for small-scale modeling (COSMO) model in Climate Mode (CCLM) is utilized as the convection permitting regional climate model[47]. The detailed CCLM configurations are provided in Table 2. The U.K. Earth System Model 1.0-LL (UKESM) is used as the lateral boundary condition, which has native N96 grid[48]. We use historical (2001–2005) and two future scenarios (2091–2095), SSP126 and SSP585, from the UKESM data for the CPM simulation. A double-nesting method is applied for dynamical downscaling of the coarse-resolution UKESM. First, the UKESM data are dynamically downscaled into 25 km resolution for the East Asia domain using CCLM (Supplementary Fig. 6). Next, the 25 km CCLM output data are additionally downscaled into 2.5 km resolution for South Korea region utilizing convection-permitting CCLM. The performance of the CCLM model configured identically to this study is described in Lee et al.[12].

Observation data

The Automated Synoptic Observing System (ASOS) in situ hourly rainfall data from the Korea Meteorological Administration (KMA) are used in this study for 1985–2014. To eliminate the spatial dependency among rain gauge data, we select specific ASOS stations based on Local Moran's I[49,50]. Local Moran's I is a statistical index which can measure a local spatial autocorrelation of a specific area with its neighbors and its statistical significance can be assessed through the permutation test. It is widely used in various fields such as geography, hydrology and meteorology to detect the similarity between spatially distributed data points[51–54]. Local Moran's I index for the i point (I_i) is defined as follows.

$$I_i = \frac{(x_i - \bar{x})\sum_{j=1}^{n}\omega_{ij}(x_j - \bar{x})}{(n-1)^{-1}\sum_{j=1}^{n}\left(x_j - \bar{x}\right)^2}$$

n is the number of ASOS stations, $\bar{x}$ is the mean value of all ASOS station data and ω is weight matrix. A high positive I_i value implies that the point is correlated with its neighbors. In this study, we calculate local Moran's I for the hourly extreme precipitation events where the amount of rainfall exceeds 99.95th percentile (31.0 mm). For each extreme precipitation event, local Moran's I is calculated based on the different distance from the event's occurrence station by assigning a weight of 1 to stations within the specified range and 0 to those outside it. (Supplementary Fig. 7). When examining the median values for each distance range, it is found that the distance at which the value is statistically insignificant at 95% confidence level is 20 km. This result well agrees with the previous studies (14–35 km) which analyze the spatial dependency of ASOS station in South Korea, despite differences in analyzed periods and time scales[51,55]. Therefore, after excluding those located on islands or where the percentage of missing values exceeded 1% and those with distances smaller than 20 km from each other, the 55 ASOS stations are finally selected (Supplementary Fig. 6b). The 25 km and 2.5 km CCLM hourly rainfall data are interpolated into the location of the ASOS stations using bilinear interpolation method.

The European Centre for Medium-Range Weather Forecasts (ECMWF) Reanalysis v5 (ERA 5) reanalysis 3-hourly data provided by ECMWF are used to detect the representative weather pattern for extreme rainfall events in observed period.

Bootstrapping

Bootstrapping method is utilized to estimate the uncertainty for the observations and CCLM data. For observation and 25 km CCLM data, we randomly select three individual years out of 30 years (1985–2014) with replacement and this process is repeated 1000 times. For 2.5 km CCLM data, due to the limited period, we randomly select three individual years out of 5 years (2001–2005 for historical climate and 2091–2095 for future climate) with replacement and this process is repeated 30 times. The 5th and 95th percentiles are calculated from each sample to determine the 90% confidence interval. To preserve the spatial relationship of the original data in the bootstrap sample, we use all stations for each bootstrap sample, rather than select individual station and apply bootstrapping for the time only[13,56].

In this manuscript, the results derived from bootstrapping are analyzed based on the median values of the annual mean. Statistical significance of the future changes compared to the historical climate is examined utilizing Wilcoxon rank-sum test.

Definition of hourly extreme rainfall event (HER)

The summertime (June to September) hourly precipitation data, derived from the observed ASOS station data and the model data which are interpolated into ASOS stations, are used to define extreme HER. In this study, we treat the each of the hourly data (5 years × 55 stations) as an individual case, disregarding temporal and spatial properties. First, the 99.95th percentile hourly precipitation is calculated from pooling of all stations data. The threshold of the 99.95 percentile (31.0 mm in the observation data) is chosen because it is comparable to 30 mm which has been used as the criterion for extreme rainfall in previous studies and KMA[6,33]. Thus, the HER is defined as the cases where the hourly-accumulated rainfall amount exceeds the threshold (99.95th percentile rainfall in historical period). The rainfall amount threshold of model derived from the historical period is adopted for both historical and future periods. Here, the HERs that occurs during the period when tropical cyclones are located in near South Korea (32–40°N, 120–138°E) are excluded since their dynamics and precipitation mechanisms differ from those of synoptic-scale systems, requiring a separate approach for analysis[57,58].

The observed tropical cyclone best-track data are provided by Regional Specialized Meteorological Center Tokyo. The model tropical cyclone tracks are detected using 25 km CCLM data following the method of previous studies[59–61], applying suitable thresholds for the CCLM. Also, in order to ensure the independence of HERs, we only consider events with a time interval of at least two hours between them at each station. The time interval threshold of the two hours is obtained through the time autocorrelation. Statistical significance at 95% confidence level disappears at two-hour when calculating autocorrelation for the period of 24 h before and after the extreme precipitation occurred time (Supplementary Fig. 7). The two-hour time interval is occasionally employed in hourly scale rainfall research in East Asia[62,63]. The sensitivity test for defining rainfall amount threshold is also conducted for data without no-rain hours or applied different time intervals, but the overall results do not change significantly.

The convective HER is defined using convective available potential energy (CAPE) values[12,64]. CAPE is the amount of energy available for convection which has been widely used as a measure of atmospheric instability. Extremely unstable environments are typically defined by CAPE > 2500 J/kg in continental regions like the U.S., but due to lower CAPE in South Korea when extreme rainfall occurs, this study adjusts the threshold to 800 J/kg to reflect regional condition[65,66]. Here, we identify the convective HER from the total rainfall events by selecting those with CAPE values exceeding 800 J/kg. CAPE is calculated from the hourly data derived from CPM which is interpolated into ASOS stations.

Self-organizing map clustering

We use self-organizing map (SOM) method to cluster the weather patterns related to the HER. SOM is a type of unsupervised artificial neural network that has a capable of mapping high-dimensional data into low-dimensional array with preserving the important topological relationships between input data[67,68]. Because of its ability to extract major signals from complex datasets, the SOM method has been widely utilized in climate sciences and meteorology[36,69–73].

In this study, we conduct the clustering of weather patterns using SOM method with reference to Hoffmann and Schlünzen[74] and Park et al.[36]. SOM method is applied to the 30 years (1985–2014) 3-hourly normalized ERA5 geopotential height at 850 hPa around South Korea (27–47°N, 112–136°E) for the time which is closest to the observed HER occurrence time. Here, the observed 1894 HER for 1985–2014 is newly calculated for clustering weather patterns. The 1 × 6 node array is selected based on several sensitivity tests to reflect the temporal variability of geopotential height. Since SOM algorithm arranges the similar clusters adjacently, the one-dimensional node array is suitable for arranging the climate data in sequence[36,75]. The SOM clustering yields six dominant weather patterns of HER. Using these six clusters as the criteria, the normalized 850 hPa geopotential height patterns for HERs derived from the RCM data are distributed into the six observed HER clusters. The normalized RCM data are calculated as follows. First, the RCM data are interpolated into the ERA5 grid. Then the interpolated RCM data are normalized with a temporal mean value of RCM data and a temporal standard deviation of the corresponding ERA5 data (1985–2014) to match the magnitude of signal with the observation. The process of sorting the normalized RCM data is conducted in the same manner as the SOM, which finds the best matching unit (BMU). The

Euclidean distance is calculated between each HER weather pattern data and the six clusters, and then the HER is assigned to the node with the smallest distance. This distribution method is conducted for both historical and future periods of RCM data with the assumption that the overall climate patterns might not change in the future.

The analyzed results of Quantization Error (QE) and topographical error (TE) are calculated using the climate data and their BMU to support this assumption (Supplementary Fig. 8). These two indices are widely used as the quality measurement of the SOM performance[76–78]. The QE is the distance data between data vector and best matching unit, which provide a basis for estimating how well the input data has been clustered. TE is proportion of all data that first and second BMUs are not adjacent vector. It measures how well the structure of the input space is modeled. In Supplementary Fig. 8b, the median of mean QE and TE for CPM data for all scenarios are in a range of observation, except QE for SSP585. The reason of the mean QE for SSP585 is out of range is that the QE in SSP585 has a secondary probability density peak around 80. However, it is noteworthy that the primary peak is still around the median of the observed QE.

Data availability

The model simulation data used in this study are available upon reasonable request from the authors. The ASOS station data are available at https://apihub.kma.go.kr. The ERA5 data can be downloaded at https://cds.climate.copernicus.eu. The observed tropical cyclone data are available at https://www.jma.go.jp/jma/jma-eng/jma-center/rsmc-hp-pub-eg/besttrack.html.

Code availability

Source codes used in this study are available from the authors upon reasonable request.

Received: 20 December 2024; Accepted: 25 April 2025;

References

1. KMA. *2021 Abnormal Climate Report*. 234 (2022).
2. KMA. *2022 Abnormal Climate Report*. 166 (2023).
3. Yilmaz, A. G. & Perera, B. J. C. Spatiotemporal Trend Analysis of Extreme Rainfall Events in Victoria, Australia. *Water Resour. Manag.* **29**, 4465–4480 (2015).
4. Xiao, C., Wu, P., Zhang, L. & Song, L. Robust increase in extreme summer rainfall intensity during the past four decades observed in China. *Sci. Rep.* **6**, 38506 (2016).
5. Fowler, H. J. et al. Anthropogenic intensification of short-duration rainfall extremes. *Nat. Rev. Earth Environ.* **2**, 107–122 (2021).
6. Do, H.-S. et al. Long-term change of summer mean and extreme precipitations in Korea and East Asia. *Int. J. Climatol.* **43**, 3476–3492 (2023).
7. Westra, S. et al. Future changes to the intensity and frequency of short-duration extreme rainfall. *Rev. Geophys.* **52**, 522–555 (2014).
8. Meredith, E. P., Maraun, D., Semenov, V. A. & Park, W. Evidence for added value of convection-permitting models for studying changes in extreme precipitation. *J. Geophys. Res. Atmos.* **120**, 12500–12513 (2015).
9. Kim, G. et al. Future changes in extreme precipitation indices over Korea. *Int. J. Climatol.* **38**, e862–e874 (2018).
10. Myhre, G. et al. Frequency of extreme precipitation increases extensively with event rareness under global warming. *Sci. Rep.* **9**, 16063 (2019).
11. Armon, M. et al. Reduced rainfall in future heavy precipitation events related to contracted rain area despite increased rain rate. *Earth's Future* **10**, e2021EF002397 (2022).
12. Lee, D. et al. Enhanced role of convection in future hourly rainfall extremes over South Korea. *Geophys. Res. Lett.* **49**, e2022GL099727 (2022).
13. Chapman, S. et al. Climate change impacts on extreme rainfall in Eastern Africa in a convection-permitting climate model. *J. Clim.* **36**, 93–109 (2023).
14. Prein, A. F. et al. A review on regional convection-permitting climate modeling: demonstrations, prospects, and challenges. *Rev. Geophys.* **53**, 323–361 (2015).
15. Lucas-Picher, P. et al. Convection-permitting modeling with regional climate models: Latest developments and next steps. *WIREs Clim. Change* **12**, e731 (2021).
16. Ban, N., Schmidli, J. & Schär, C. Evaluation of the convection-resolving regional climate modeling approach in decade-long simulations. *J. Geophys. Res. Atmos.* **119**, 7889–7907 (2014).
17. Fosser, G., Khodayar, S. & Berg, P. Benefit of convection permitting climate model simulations in the representation of convective precipitation. *Clim. Dyn.* **44**, 45–60 (2015).
18. Kendon, E. J. et al. Do Convection-permitting regional climate models improve projections of future precipitation change? *Bull. Am. Meteorol. Soc.* **98**, 79–93 (2017).
19. Zhao, Y., Zhou, T., Li, P., Furtado, K. & Zou, L. Added value of a convection permitting model in simulating atmospheric water cycle over the asian water tower. *J. Geophys. Res. Atmos.* **126**, e2021JD034788 (2021).
20. Woodhams, B. J. et al. What is the added value of a convection-permitting model for forecasting extreme rainfall over tropical East Africa?. *Mon. Weather Rev.* **146**, 2757–2780 (2018).
21. Luu, L. N., Vautard, R., Yiou, P. & Soubeyroux, J. M. Evaluation of convection-permitting extreme precipitation simulations for the south of France. *Earth Syst. Dyn.* **13**, 687–702 (2022).
22. Médus, E. et al. Characteristics of precipitation extremes over the Nordic region: added value of convection-permitting modeling. *Nat. Hazards Earth Syst. Sci.* **22**, 693–711 (2022).
23. Weusthoff, T., Ament, F., Arpagaus, M. & Rotach, M. W. Assessing the benefits of convection-permitting models by neighborhood verification: examples from MAP D-PHASE. *Mon. Weather Rev.* **138**, 3418–3433 (2010).
24. Prein, A. F. et al. Added value of convection permitting seasonal simulations. *Clim. Dyn.* **41**, 2655–2677 (2013).
25. Reder, A., Raffa, M., Montesarchio, M. & Mercogliano, P. Performance evaluation of regional climate model simulations at different spatial and temporal scales over the complex orography area of the Alpine region. *Nat. Hazards* **102**, 151–177 (2020).
26. Dallan, E. et al. How well does a convection-permitting regional climate model represent the reverse orographic effect of extreme hourly precipitation?. *Hydrol. Earth Syst. Sci.* **27**, 1133–1149 (2023).
27. Jung, H.-S., Lim, G.-H. & Oh, J.-H. Interpretation of the transient variations in the time series of precipitation amounts in Seoul, Korea. Part I: diurnal variation. *J. Clim.* **14**, 2989–3004 (2001).
28. Park, C., Son, S.-W. & Kim, H. Distinct features of atmospheric rivers in the early versus late East Asian Summer Monsoon and their impacts on monsoon rainfall. *J. Geophys. Res. Atmos.* **126**, e2020JD033537 (2021).
29. Shin, U., Park, S.-H., Yun, Y.-R. & Oh, C. Synoptic features of august heavy rainfall episodes accompanied by a quasi-stationary front over the Korean Peninsula and its relationship with the Western Pacific Subtropical High. *Front. Earth Sci*. **10** (2022).
30. Lee, J.-Y. et al. The long-term variability of Changma in the East Asian summer monsoon system: A review and revisit. *Asia-Pac. J. Atmos. Sci.* **53**, 257–272 (2017).
31. Choi, J.-W., Kim, H.-D. & Wang, B. Interdecadal variation of Changma (Korean summer monsoon rainy season) retreat date in Korea. *Int. J. Climatol.* **40**, 1348–1360 (2020).
32. KMA. *White paper on Changma 2022*. 394 (2022).
33. Jo, E. et al. Classification of localized heavy rainfall events in South Korea. *Asia-Pac. J. Atmos. Sci.* **56**, 77–88 (2019).

34. Jin, H.-G., Lee, H. & Baik, J.-J. Characteristics and possible mechanisms of diurnal variation of summertime precipitation in South Korea. *Theor. Appl. Climatol.* **148**, 551–568 (2022).
35. Knist, S., Goergen, K. & Simmer, C. Evaluation and projected changes of precipitation statistics in convection-permitting WRF climate simulations over Central Europe. *Clim. Dyn.* **55**, 325–341 (2020).
36. Park, C. et al. Diverse synoptic weather patterns of warm-season heavy rainfall events in South Korea. *Mon. Weather Rev.* **149**, 3875–3893 (2021).
37. Kim, Y.-H., Min, S.-K., Zhang, X., Sillmann, J. & Sandstad, M. Evaluation of the CMIP6 multi-model ensemble for climate extreme indices. *Weather Clim. Extremes* **29**, 100269 (2020).
38. Nijsse, F. J. M. M., Cox, P. M. & Williamson, M. S. Emergent constraints on transient climate response (TCR) and equilibrium climate sensitivity (ECS) from historical warming in CMIP5 and CMIP6 models. *Earth Syst. Dyn.* **11**, 737–750 (2020).
39. Senior, C. A. et al. U.K. Community earth system modeling for CMIP6. *J. Adv. Model. Earth Syst.* **12**, e2019MS002004 (2020).
40. He, C. & Zhou, T. Responses of the Western North Pacific subtropical high to global warming under RCP4.5 and RCP8.5 scenarios projected by 33 CMIP5 models: the dominance of Tropical Indian Ocean–Tropical Western Pacific SST gradient. *J. Clim.* **28**, 365–380 (2015).
41. Huang, D., Liu, A., Zheng, Y. & Zhu, J. Inter-model spread of the simulated East Asian Summer Monsoon rainfall and the associated atmospheric circulations from the CMIP6 models. *J. Geophys. Res. Atmos.* **127**, e2022JD037371 (2022).
42. Lu, K., He, J. & Simpson, I. R. Origins of uncertainty in the response of the summer north pacific subtropical high to CO_2 forcing. *Geophys. Res. Lett.* **50**, e2023GL105042 (2023).
43. Chen, X., Zhou, T., Wu, P., Guo, Z. & Wang, M. Emergent constraints on future projections of the western North Pacific Subtropical High. *Nat. Commun.* **11**, 2802 (2020).
44. Jo, S.-Y. et al. Hysteresis behaviors in east asian extreme precipitation frequency to CO_2 pathway. *Geophys. Res. Lett.* **49**, e2022GL099814 (2022).
45. Hatsuzuka, D. & Sato, T. Future changes in monthly extreme precipitation in japan using large-ensemble regional climate simulations. *J. Hydrometeorol.* **20**, 563–574 (2019).
46. Wang, C.-Y., Zheng, X.-T. & Song, F. Enhanced mid-to-late summer precipitation over midlatitude East Asia under global warming. *J. Clim.* **37**, 4221–4237 (2024).
47. Rockel, B., Will, A. & Hense, A. The regional climate model COSMO-CLM (CCLM). *Meteorol. Z.* **17**, 347 (2008).
48. Sellar, A. A. et al. UKESM1: description and evaluation of the U.K. earth system model. *J. Adv. Model. Earth Syst.* **11**, 4513–4558 (2019).
49. Moran, P. A. The interpretation of statistical maps. *J. R. Stat. Soc. Ser. B-Stat. Methodol.* **10**, 243–251 (1948).
50. Anselin, L. Local Indicators of Spatial Association—LISA. *Geogr. Anal.* **27**, 93–115 (1995).
51. Park, S., Park, S. K., Lee, J. W. & Park, Y. Geostatistical assessment of warm-season precipitation observations in Korea based on the composite precipitation and satellite water vapor data. *Hydrol. Earth Syst. Sci.* **22**, 3435–3452 (2018).
52. Xu, L., Zheng, C. & Ma, Y. Variations in precipitation extremes in the arid and semi-arid regions of China. *Int. J. Climatol.* **41**, 1542–1554 (2021).
53. Liu, Y., Tian, J., Zheng, W. & Yin, L. Spatial and temporal distribution characteristics of haze and pollution particles in China based on spatial statistics. *Urban Clim.* **41**, 101031 (2022).
54. Yeh, H.-F., Chang, J.-C., Huang, C.-C. & Chen, H.-Y. Spatial correlation of groundwater level with natural factors using geographically weighted regression model in the Choushui River Alluvial Fan, Taiwan. *Front. Earth Sci*. **10** (2022).
55. Park, S., Lee, Y.-H., Ahn, K.-D. & Lee, S.-W. A study on the characteristic distance (e-folding distance) of summer precipitation over the Korean Peninsula using reanalysis data. In: *Proc. Autumn Meeting, Korean Meteorological Society*, OCT 29-31, 146 (2018). (in Korean)
56. Hanel, M., Buishand, T. A. & Ferro, C. A. T. A nonstationary index flood model for precipitation extremes in transient regional climate model simulations. *J. Geophys. Res. Atmos*. **114** (2009).
57. Chen, J.-M., Li, T. & Shih, C.-F. Tropical cyclone– and monsoon-induced rainfall variability in Taiwan. *J. Clim.* **23**, 4107–4120 (2010).
58. Son, C., Lee, T. & Kwon, H. -h Integrating nonstationary behaviors of typhoon and non-typhoon extreme rainfall events in East Asia. *Sci. Rep.* **7**, 5097 (2017).
59. Cha, D.-H., Jin, C.-S., Lee, D.-K. & Kuo, Y.-H. Impact of intermittent spectral nudging on regional climate simulation using Weather Research and Forecasting model. *J. Geophys. Res.* **116**, D10103 (2011).
60. Jin, C.-S. et al. Evaluation of climatological tropical cyclone activity over the western North Pacific in the CORDEX-East Asia multi-RCM simulations. *Clim. Dyn.* **47**, 765–778 (2016).
61. Lee, M. et al. Comparison of tropical cyclone activities over the Western North Pacific in CORDEX-East Asia phase I and II experiments. *J. Clim.* **33**, 10593–10607 (2020).
62. Li, J., Yu, R. & Sun, W. Duration and seasonality of hourly extreme rainfall in the central eastern China. *Acta Meteorol. Sin.* **27**, 799–807 (2013).
63. Tu, A., Zeng, J., Liu, Z., Zheng, H. & Xie, S. Effect of minimum inter-event time for rainfall event separation on rainfall properties and rainfall erosivity in a humid area of southern China. *Geoderma* **431**, 116332 (2023).
64. Purr, C., Brisson, E. & Ahrens, B. Convective rain cell characteristics and scaling in climate projections for Germany. *Int. J. Climatol.* **41**, 3174–3185 (2021).
65. Song, H.-J. Long-term variations of cloud top patterns associated with heavy rainfall over the Korean peninsula. *J. Hydrol. Reg. Stud.* **46**, 101337 (2023).
66. Jung, S.-P. et al. Thermodynamic characteristics associated with localized torrential rainfall events in the southwest region of the Korean peninsula. *Asia-Pac. J. Atmos. Sci.* **51**, 229–237 (2015).
67. Kohonen, T. The self-organizing map. *Proc. IEEE* **78**, 1464–1480 (1990).
68. Wickramasinghe, C. S., Amarasinghe, K. & Manic, M. Deep self-organizing maps for unsupervised image classification. *IEEE Trans. Ind. Inf.* **15**, 5837–5845 (2019).
69. Malmgren, B. A. & Winter, A. Climate zonation in puerto rico based on principal components analysis and an artificial neural network. *J. Clim.* **12**, 977–985 (1999).
70. Hewitson, B. C. & Crane, R. G. Self-organizing maps: applications to synoptic climatology. *Clim. Res.* **22**, 13–26 (2002).
71. Johnson, N. C., Feldstein, S. B. & Tremblay, B. The continuum of Northern Hemisphere teleconnection patterns and a description of the NAO shift with the use of self-organizing maps. *J. Clim.* **21**, 6354–6371 (2008).
72. Oettli, P., Tozuka, T., Izumo, T., Engelbrecht, F. A. & Yamagata, T. The self-organizing map, a new approach to apprehend the Madden–Julian Oscillation influence on the intraseasonal variability of rainfall in the southern African region. *Clim. Dyn.* **43**, 1557–1573 (2014).
73. Baiman, R., Winters, A. C., Lenaerts, J. & Shields, C. A. Synoptic drivers of atmospheric river induced precipitation near Dronning Maud Land, Antarctica. *J. Geophys. Res. Atmos.* **128**, e2022JD037859 (2023).
74. Hoffmann, P. & Schlünzen, K. H. Weather pattern classification to represent the urban heat island in present and future climate. *J. Appl. Meteorol. Climatol.* **52**, 2699–2714 (2013).

75. Kohonen, T. The self-organizing map. *Neurocomputing* **21**, 1–6 (1998).
76. Doan, Q. V., Kusaka, H., Sato, T. & Chen, F. S-SOM v1.0: a structural self-organizing map algorithm for weather typing. *Geosci. Model Dev.* **14**, 2097–2111 (2021).
77. Nguyen-Le, D., Yamada, T. J. & Tran-Anh, D. Classification and forecast of heavy rainfall in northern Kyushu during Baiu season using weather pattern recognition. *Atmos. Sci. Lett.* **18**, 324–329 (2017).
78. Nowak-Brzezińska, A. & Horyń, C. Self-Organizing Map algorithm as a tool for outlier detection. *Proced. Comput. Sci.* **207**, 2162–2171 (2022).

Acknowledgements

This study was supported by the Korea Meteorological Administration Research and Development Program under Grant RS-2024-00403386, and the Human Resource Program for Sustainable Environment in the 4th Industrial Revolution Society. We acknowledge the members of the Climate Limited-area Modelling Community (CLM-Community) for their help in setting up the CCLM simulations. The CCLM simulations were performed by using the supercomputing resource of the Korea Meteorological Administration (National Center for Meteorological Supercomputer).

Author contributions

S.K.M. and G.Y.S. conceived the study. G.Y.S. led the analysis of model outputs and the manuscript writing. D.L. performed model experiments. S.W.S., C.P., and D.H.C. contributed to the interpretation of results and the manuscript writing.

Competing interests

The authors declare no competing interests.

Additional information

Supplementary information The online version contains supplementary material available at https://doi.org/10.1038/s41612-025-01067-z.

Correspondence and requests for materials should be addressed to Seung-Ki Min.

Reprints and permissions information is available at http://www.nature.com/reprints